Available online at www.sciencedirect.com
ScienceDirect
Trans. Nonferrous Met. Soc. China 28(2018) 1543−1552
Transactions of Nonferrous Metals Society of China
www.tnmsc.cn

Zr−Co(Cu)−Al bulk metallic glasses with optimal glass-forming ability and their compressive properties

Masoud MOHAMMADI RAHVARD, Morteza TAMIZIFAR, Seyed Mohammad Ali BOUTORABI

School of Materials Science and Engineering, Center of Excellence for High Strength Alloys Technology, Iran University of Science and Technology, Tehran 1684613114, Iran

Received 10 July 2017; accepted 4 January 2018

Abstract: The formation of bulk metallic glasses (BMGs) in the ternary $Zr_{56}Co_{28}Al_{16}$ and quaternary $Zr_{56}Co_{28-x}Cu_xAl_{16}$ (x=2, 4, 5, 6, 7, mole fraction, %) glassy alloys was investigated via the copper mold suction casting method. The main purpose of this work was to locate the optimal BMG-forming composition for the quaternary ZrCo(Cu)Al alloys and to improve the plasticity of the parent alloy. The X-ray diffractometry (XRD), transmission electron microscopy (TEM) and differential scanning calorimetry (DSC) were used to investigate the glassy alloys structure and their glass forming ability (GFA). In addition, the compression test, microhardness, nano-indentation and scanning electron microscopy (SEM) were utilized to discuss the possible mechanisms involved in the enhanced plasticity achievement. The highest GFA among Cu-containing alloys was found for the $Zr_{56}Co_{22}Cu_6Al_{16}$ alloy, which was similar to that of the base alloy. Furthermore, the plasticity of the base alloy increased significantly from 3.3% to 6% for the $Zr_{56}Co_{22}Cu_6Al_{16}$ BMG. The variations in the plasticity and GFA of the alloys were discussed by considering the positive heat of mixing within Cu and Co elements.

Key words: bulk metallic glass; zirconium base alloy; glass forming ability; plasticity

1 Introduction

The Zr-based bulk metallic glasses (BMGs) have been widely used for the structural applications in recent two decades due to excellent properties such as high glass forming ability (GFA), superior mechanical properties, good corrosion resistance, good bio-compatibility and high wear resistance [1,2]. However, the deformation of BMGs under mechanical loading is highly localized in the shallow shear band region as a result of shear softening, leading to a catastrophic failure with limited plastic strain. Therefore, their applications and processing methods are limited severely due to their poor room-temperature plasticity [3,4]. In order to broaden the application of BMGs and overcome the intrinsic brittleness of BMGs, various methods such as the in-situ or ex-situ introduction of the second crystalline phase into the glassy matrix, excessive free-volume embedded in the structure, enhancement of the Poisson ratio, and heterogeneous structure have been applied [5−8]. All of these can be easily achieved by means of minor element addition. In addition, the minor addition can generally improve GFA of BMGs by stabilizing the liquid phase or destabilizing the competing crystalline phases during solidification [9,10]. Thus, the minor addition can be used as a promising way to explore the new BMG with outstanding mechanical properties or high GFA.

Zr-based BMGs have been developed in various alloy systems. Among different Zr-based BMGs, the ternary Zr−Co−Al alloy system, as compared to other Zr-based glassy alloys, possesses better properties, including high fracture strength exceeding 2 GPa and toxic elements free like Ni and Be, which make it a possibly good candidate for biomedical applications [11,12]. WADA et al [13] systematically investigated Zr−Co−Al glassy alloy system and finally succeeded in synthesizing $Zr_{56}Co_{28}Al_{16}$ BMG with the highest GFA among the ternary Zr−Co−Al glassy alloys. Numerous researches have been carried out to tune the composition and properties, especially GFA and plasticity, which are important features for applications. Previous studies found that Cu can improve GFA of the Zr−Co−Al-based BMGs. For example, ZHANG and INOUE [14] succeeded in synthesizing $Zr_{55}Al_{20}Co_{20}Cu_5$

Corresponding author: Morteza TAMIZIFAR; Tel: +98-9121003313; Fax: +98-2177240480; E-mail: tamizifar@iust.ac.ir
DOI: 10.1016/S1003-6326(18)64796-X

BMG by optimizing the composition of the quaternary $Zr_{55}Al_{20}Co_{25-x}Cu_x$ (x=0, 5, 10, 15) glassy alloys. They merely investigated the effect of Cu major addition on the GFA of Zr−Co−Al-based BMGs. It is noteworthy that the compressive plasticity and GFA of quaternary Zr−Co−Cu−Al alloy have not been studied in detail at all.

It is well-known that the structure of the parent amorphous phase has a significant influence on the properties. Thus, the enhancement of GFA and plasticity, and their correlation with the structure have been elaborated. In this work, we systematically investigated the effect of the minor substitution of Co with Cu (mole fractions of Cu are 0, 2%, 4%, 5%, 6% and 7%) on the GFA and plasticity by varying the composition of $Zr_{56}Co_{28-x}Cu_xAl_{16}$ BMG. Zr-based $Zr_{56}Co_{28}Al_{16}$ metallic glass has been selected since it has the highest GFA among the Zr−Co−Al glassy alloy system. This work was performed with the aim of fabricating the monolithic BMG with intrinsic plasticity and locating the optimal BMG-forming composition for the quaternary Zr−Co(Cu)−Al glassy alloy, which is potentially favorable for the biomedical applications. The highest GFA among glassy alloys was found for the $Zr_{56}Co_{22}Cu_6Al_{16}$ alloy. Furthermore, the plasticity of the base alloy increased significantly for the optimized Cu-containing alloy. It should be noted that this work has focused extensively on the internal state evolution to study the possible mechanisms involved in the plasticity and GFA variations.

2 Experimental

A series of $Zr_{56}Co_{28-x}Cu_xAl_{16}$ (x= 0, 2, 4, 5, 6 and 7, mole fraction, %) alloy ingots, denoted as Z, C2, C4, C5, C6 and C7 respectively, were prepared via arc melting the high-purity constituent elements, namely Zr (99.9%), Co (99.99%), Al (99.999%), Cu (99.999%), under the Ti-gettered high-purity argon atmosphere. The ingots were remelted four times to ensure compositional homogeneity. Then, rods with different diameters and 5 cm in length were fabricated via water-cooled copper mold suction casting method. The structure of as-cast rods was examined by X-ray diffractometry (XRD, PANalytical X'Pert PRO diffraction, Cu K_α radiation) and transmission electron microscopy (TEM, FEI Tecnai G2 F20 200 kV Cryo-STEM). TEM samples were prepared using the dual beam FIB system. The thermal behavior of samples was characterized using differential scanning calorimetry (TG−DSC, Setaram, France) under a continuous helium flow at a heating rate of 0.67 K/s and differential thermal analysis (TG−DTA, Bahr STA 503, Germany) under a continuous argon flow at a heating rate of 0.33 K/s.

The nano-indentation test was performed on the as-cast samples by the nono-indentation tester with Berkovich diamond tip under the loading rate of 100 μN/s and the load limit of 10 mN. The microhardness test was performed on the as-cast and as-annealed samples on the Leitz machine with a load of 100 g and a holding time of 10 s. At least five points were measured to ensure statistical reliability of the data. The structural relaxation heat treatment was performed in the resistance furnace under high-purity argon atmosphere at 70 °C below T_g (T_g is the glass transition temperature) and a holding time of 2 h for the samples placed in the vacuumed sealed quartz tube. The density of samples was measured using Archimedean principles on an electrical balance (Sartorius) with an accuracy of 0.0001 g. At least three times were measured to ensure statistical reliability of the data. The mechanical properties were measured by the room temperature compression test performed on an instrument (Santam, Iran) at low strain rate of 3×10^{-4} s^{-1}. The dimensions of specimens for the compression test were 1.5 mm in diameter and 3 mm in length with aspect ratio of 2:1 according to ASTM: E9−09 standard. The specimens were cut from the as-cast rods by a low-speed saw and then both the top and bottom sides of the sample were carefully polished to ensure parallelism. The compression test was repeated at least three times for each sample. The fracture surface morphology and lateral surface of fractured samples were investigated by scanning electron microscopy (SEM-Vega Tescan).

3 Glass forming ability

3.1 Structural analysis

The XRD patterns of the as-cast $Zr_{56}Co_{28-x}Cu_xAl_{16}$ (x=0, 2, 4, 5, 6, 7) BMGs with a diameter of 2 mm are shown in Fig. 1. As can be seen, there exists a broad halo peak in 2θ range of 35°−40°, yet no other diffraction peaks of crystalline phases are observed for Z and C6 samples, indicating the fully amorphous phase within the XRD instrument resolution limit. However, some detectable diffraction peaks on the broad peak, corresponding to the crystalline phase in the C2, C4, C5 and C7 samples, are observed. Furthermore, the intensity of peaks, revealing the volume fraction of crystalline phases, has clearly been decreased upon Cu addition up to the optimum chemical composition and then has been increased by further Cu addition. Based on the phase analysis results, there is an optimal Cu amount, at which the GFA reaches the maximum value and then drops by further adding the Cu element such that the highest GFA is found for the C6 sample. One can find that GFA of $Zr_{56}Co_{22}Cu_6Al_{16}$ glassy alloy remains more or less similar to that of $Zr_{56}Co_{28}Al_{16}$, in spite of micro alloying an element with the positive heat of mixing.

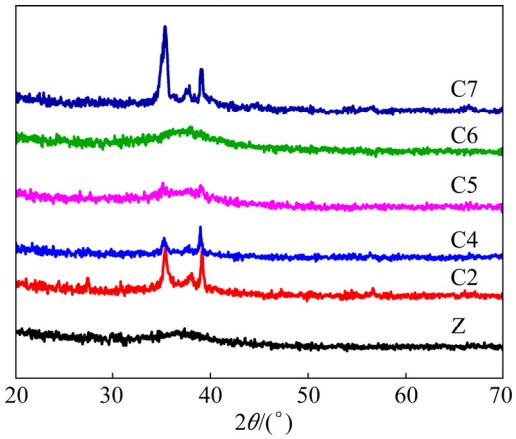

Fig. 1 XRD patterns of as-cast $Zr_{56}Co_{28-x}Cu_xAl_{16}$ (x=0, 2, 4, 5, 6, 7) BMGs with diameter of 2 mm

Noticeably, the critical diameter d_c of the glassy rods can be promoted by other casting methods such as injection and tilt casting, e.g., $Zr_{56}Co_{28}Al_{16}$ BMG with d_c of 18 mm can be fabricated via the tilt casting method [13]. The present work has merely been performed to optimize the composition to achieve the highest GFA among ZrCoCuAl glassy alloys; thus, future works need to explore the critical diameter of glassy alloy by varying the solidification conditions such as the casting method or processing parameters.

Figure 2 shows the bright-field TEM/HRTEM images and selected area electron diffraction (SAED) patterns of the as-cast Z and C6 glassy rods with a diameter of 2 mm. The uniform featureless contrast in the images and a broad halo in the SAED patterns confirm amorphous nature of the samples.

It is well-known that the glassy-forming alloys should follow three empirical Inoue rules for glass formation: 1) the multicomponent system with at least three components, 2) a significant atomic size difference ratio above 12%, and 3) the negative mixing enthalpy between the constituents. These glass-forming alloys have special features as follows: 1) the higher degrees of dense randomly packed atomic configurations, 2) the new local atomic configurations, which are different from those of the corresponding crystalline phases, and 3) a homogeneous atomic configuration of the multi-component on a long range scale.

It should be mentioned that the combination of these features leads to the higher crystallization resistance of the super-cooled liquid, resulting in higher GFA for the following reasons: 1) a decrease in the atomic diffusivity and an increase in super-cooled liquid viscosity, leading to higher T_g, 2) an increase in the solid/liquid interfacial energy, leading to a decrease in the nucleation rate, and 3) a necessity for the long-range diffusion of atoms, leading to a decrease in the growth of crystalline phases [15,16].

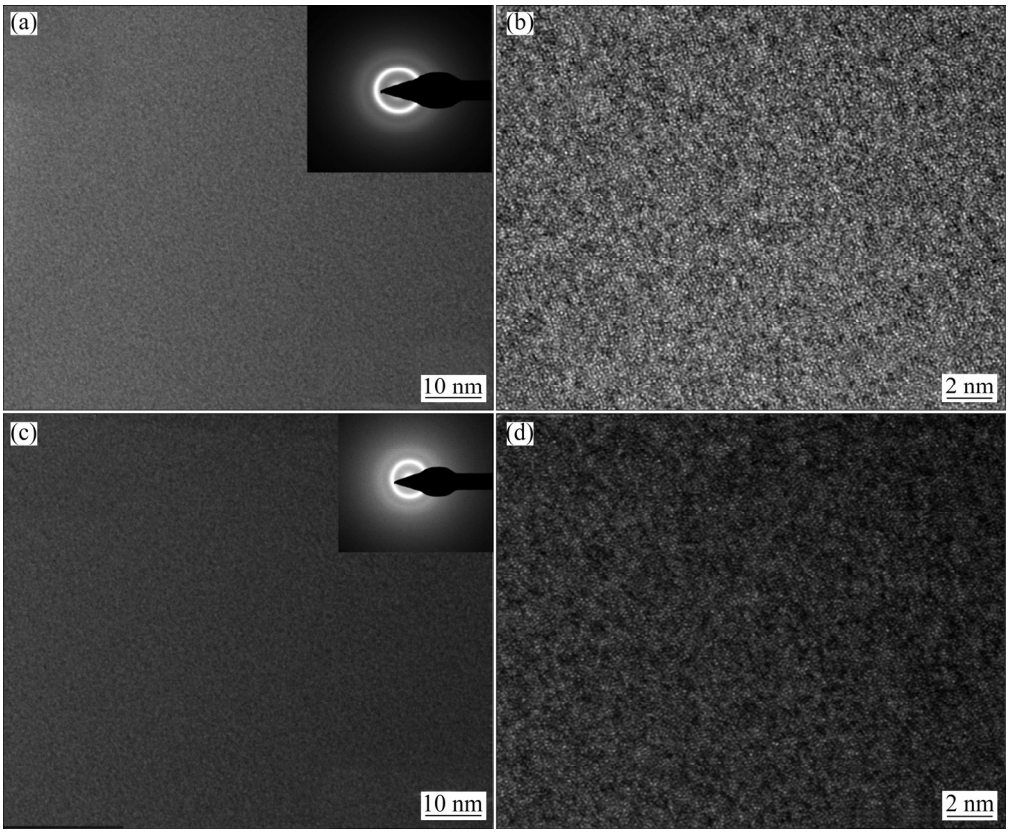

Fig. 2 Bright-field TEM/HRTEM images and selected area electron diffraction (SAED) patterns of as-cast Z (a, b) and C6 (c, d) glassy rods

In order to examine the GFA of glassy alloys closely, we have presented a possible explanation from the atomic structural perspective. The atomic size and mixing enthalpy of the constituents of ZrCoCuAl glassy alloy are shown in Fig. 3. According to the first empirical Inoue rules, the multicomponent glassy alloy has been obtained with Cu addition. Yet, the second rule has not been satisfied because of the marginal mismatch of Co and Cu. Cu with small radius and with a size similar to that of Co does not make a more sequential change to the atomic size such that Zr≫Al≫Co=Cu. Thus, it seems that the Cu addition would not affect the packing state of glassy alloy.

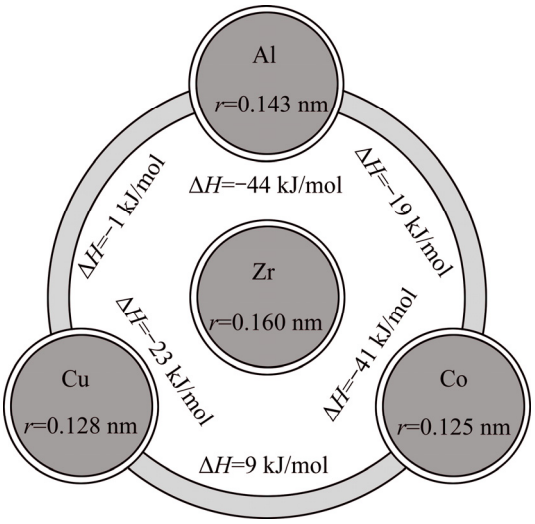

Fig. 3 Mixing enthalpy and atomic radius of constituent of ZrCoCuAl glassy alloy

Furthermore, the alloy mixing enthalpy has been decreased as result of the positive mixing enthalpy of the $\Delta H^{\text{mix}}_{\text{Cu-Co}}$, as well as the lower $\Delta H^{\text{mix}}_{\text{Cu-Zr}}$ and $\Delta H^{\text{mix}}_{\text{Cu-Al}}$, as compared to the $\Delta H^{\text{mix}}_{\text{Co-Zr}}$ and $\Delta H^{\text{mix}}_{\text{Co-Al}}$.

The mixing enthalpy and microhardness of the alloys are shown in Fig. 4. The microhardness and mixing enthalpy variations show a decrement trend by increasing the Cu content.

The mixing enthalpy of alloys could be calculated as follows [17]:

$$\Delta H^{\text{mix}} = \sum_{i \neq j} 4\Delta H^{\text{mix}}_{ij} x_i x_j \quad (1)$$

Based on the decrease of the mixing enthalpy and

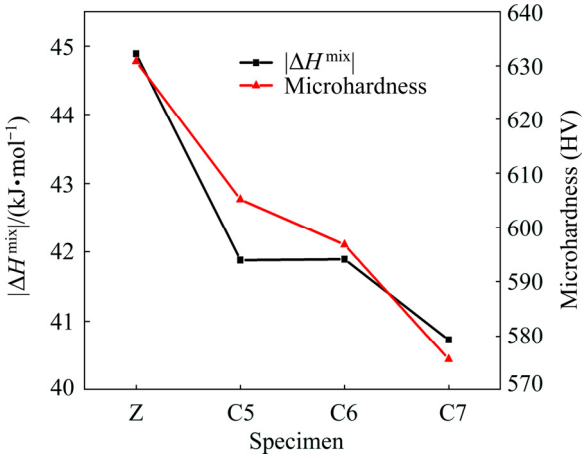

Fig. 4 Mixing enthalpy and microhardness of Z, C5, C6 and C7 glassy alloys

marginal atomic size mismatch of Cu-containing glassy alloys, it is expected that the glassy alloy with a less dense packing state would be formed. Furthermore, the microhardness decrease along with the mixing enthalpy decrease can prove the formation of a structure with a less dense randomly packed state or without any polytetrahedral packed cluster such as icosahedral short-range ordering (ISRO).

As can be seen in Table 1, in order to examine the structure closely, the microhardness and density of the Z and C6 samples have been measured in the as-cast and as-structural relaxation states. An increase in the microhardness difference from 10% for the Z sample to 15% for the C6 sample indicates that the excessive free-volume in the structure of the C6 sample has been annihilated through structural relaxation treatment. In addition, the density variations also show the same result as mentioned above. One can find that the Cu addition changes the atomic configuration of base alloy, leading to the less dense packing structure.

The excessive free-volume in the structure or less dense packing structure for the Cu-containing alloys leads to a decrease in the T_g and liquid viscosity. Based on the Turnbull crystallization kinetic theory, the nucleation rate increases by decreasing the liquid shear viscosity, providing favourable conditions for crystallization during solidification and finally resulting in lower GFA [18]. Also, based on the third empirical Inoue rule, it can be predicted that GFA for the ZrCoCuAl glassy alloy would be reduced due to the

Table 1 Microhardness and density of Z and C6 samples at as-cast and as-structural relaxation states

Sample	ρ/(g·cm^{-3})		$(\Delta\rho/\rho)$/%	Hardness (HV)		$(\Delta H_V/H_V)$/%
	As-cast	Relaxed		As-cast	Relaxed	
Z	6.6837±0.056	6.7648±0.023	1.2	630.8	698.66	~10
C6	6.7480±0.052	6.8437±0.026	1.4	596.8	702.66	~15

mixing enthalpy decrease of glassy alloys and subsequent less dense packing structure formation. However, it has been surprisingly observed that GFA of $Zr_{56}Co_{22}Cu_6Al_{16}$ glassy alloy is similar to that of the parent alloy. The reasons for this will be discussed in the next sections.

3.2 Thermal analysis

Figures 5(a) and (b) show the DSC and DTA curves for the fully amorphous samples with a diameter of 1 mm of $Zr_{56}Co_{28-x}Cu_xAl_{16}$ (x=0, 5, 6, 7) BMGs at heating rates of 0.67 and 0.33 K/s, respectively. The DSC curves exhibit the endothermic peak, characteristic of glass transition to super-cooled liquid temperature T_g, followed by two-step exothermic peak corresponding to the crystallization processes. Also, DTA curves exhibit the endothermic peak corresponding to the melting process. The characteristic temperatures, i.e., the glass transition temperature T_g, onset crystallization peak T_x, onset melting temperature T_m and liquid temperature T_l have been marked by arrows in the figures and summarized in Table 2.

The significant change in the thermal behavior has not been observed by varying the Cu content. Only the values of T_g and T_x decrease little upon Cu addition. However, a slight increase in T_g for the C6 sample, as compared to that of the C5 and C7 samples, has been observed. Also, the DTA curves show that the characteristic temperatures and peak width T_l−T_m have not been changed distinctively upon Cu addition, indicating that the compositions of glassy alloys are close to eutectic.

The reasons why the GFA is improved at the composition closer to eutectic can be considered through the thermodynamic and kinetic approach. From the thermodynamic point of view, the nucleation driving force, i.e., Gibbs free energy between the super-cooled liquid and competitive crystalline phase is lower in eutectic, as compared to the off-eutectic composition. Also, from the kinetic point of view, a number of crystalline phases begin competing with one another for the nucleation and growth in the eutectic composition, requiring extensive atomic fluctuation and rearrangement to form the crystalline phases [19]. Therefore, by the proper adjustment of the liquid composition closer to the eutectic, the liquid can be transformed into the glassy state without crystallization during solidification. ZHANG and INOUE [14] succeeded in synthesizing $Zr_{55}Al_{20}Co_{20}Cu_5$ BMG by optimizing the composition of the quaternary $Zr_{55}Al_{20}Co_{25-x}Cu_x$ (x=0, 5, 10, 15) glassy alloys. It was suggested that the composition of this alloy should be located close to the eutectic. Thus, the reasonable GFA for the Z and C6 samples can be attributed to this fact in accordance with the DTA results and a composition similar to that of the above-mentioned glassy alloy.

A number of GFA indicators in the literature, which have been formulated to predict GFA of glassy alloys

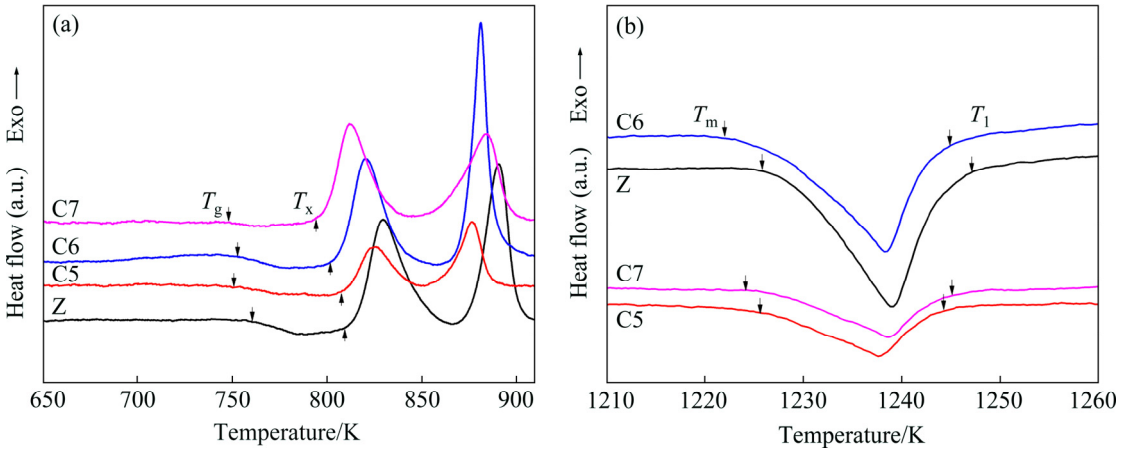

Fig. 5 DSC curves at heating rate of 0.67 K/s (a) and DTA curves at heating rate of 0.33 K/s (b) for $Zr_{56}Co_{28-x}Cu_xAl_{16}$ (x=0, 5, 6, 7) BMGs

Table 2 Characteristic temperatures, GFA indicators and critical diameters of Z, C5, C6 and C7 samples

Sample code	T_g/K	T_x/K	T_m/K	T_l/K	GFA indicator					d_c/mm
					γ	T_{rg}	K	β_1	δ	
Z	760	810	1226	1247	0.403	0.609	0.120	1.675	1.656	2
C5	750	808	1226	1244	0.405	0.602	0.138	1.680	1.622	<1.5
C6	753	802	1222	1245	0.401	0.604	0.116	1.669	1.613	2
C7	748	794	1224	1245	0.398	0.600	0.106	1.662	1.591	1

$\gamma=T_x/(T_g+T_l)$; $T_{rg}=T_g/T_l$; $K=(T_x-T_g)/(T_m-T_g)$; $\beta_1=T_x/T_g+T_g/T_l$; $\delta=T_x/(T_l-T_g)$

along with d_c, have been summarized in Table 2 [20]. As can be seen, GFA indicators do not show a reliable correlation between GFA of the alloys and d_c. The unreliable correlation between GFA and critical size for glass formation was observed in other works, especially for glassy alloys with immiscible element pairs [21].

It is expected that the Cu micro-alloying with a large positive heat of mixing between Cu and Co atoms leads to degradation in GFA since the repulsive chemical interaction causes the segregation of component atoms and finally increases the system potential energy [21]. However, the present results showed that the appropriate Cu addition can improve or does not degrade the GFA of parent alloy.

The main reason for the GFA improvement of the C6 sample, as compared to that of the other Cu-containing alloy could be attributed to Egami theory [22]. According to this theory, introducing the repulsive interaction between small atoms and increasing the interaction between the small and large atoms would favor the BMG formation. In this glassy alloy, Cu and Co atoms with smaller atomic sizes, as compared to those of Zr and Al atoms have the positive heat of mixing ($\Delta H^{\mathrm{mix}}_{\mathrm{Cu-Co}} = 9$ kJ/mol). The Cu addition in the certain composition range $0 \le x \le 6$ causes the Co atom to be attracted to large atoms, such as Zr and Al through the negative heat of mixing. Thus, this phenomenon leads to a decrease in the mobility of the Co atom for rearrangement, resulting in GFA improvement. It is noteworthy that Egami theory works better by increasing the Cu content in the certain composition range $0 \le x \le 6$ as a result of the extensive repulsive interaction along with lower direct contact between Cu and Co atoms. However, the direct contact between Cu and Co atoms would be inevitable by further adding the Cu element up to 7% (mole fraction), which destabilizes the liquid and finally deteriorates the GFA. A similar phenomenon has been reported by LIU et al [23,24] for $(Zr_{0.62}Cu_{0.23}Fe_{0.05}Al_{0.10})_{97}Ag_3$ and $Zr_{53}Co_{18.5}Al_{23.5}Ag_5$ glassy alloys with the positive heat of mixing between constituents. Another possible reason for the Cu-containing alloy GFA improvement, as compared to that for the base alloy could be attributed to "confusion principle", which expresses that the multicomponent alloy systems have a lower chance to select the viable structures [25].

4 Mechanical properties

4.1 Compression test

The compressive stress−strain curves of the Z and C6 samples with a diameter of 1.5 mm are shown in Fig. 6. As can be seen, the yield strength with a value of 2010 MPa and the ultimate strength with a value of 2320 MPa for the Z sample decrease to the values of 1710 MPa and 2080 MPa for the C6 sample, respectively. The decrease in the yield strength and ultimate strength is consistent with a decrease in the total mixing enthalpy and microhardness of the C6 glassy alloy. The comparison between the plastic strains of samples shows an increase in the plastic strain from the value of 3.3% for the Z sample to 6% for the C6 sample. It is noteworthy that the significant change in the plasticity for the monolithic BMG has been obtained by composition adjusting.

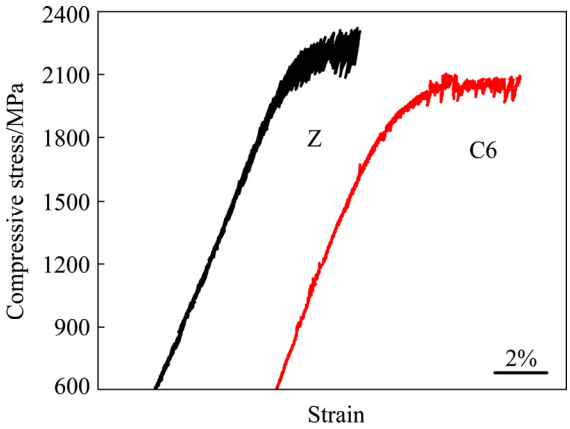

Fig. 6 Compressive stress−strain curves of Z and C6 samples with diameter of 1.5 mm at strain rate of 3×10^{-4} s^{-1}

The results have demonstrated that the serrated flow behavior is extremely different between the Z and C6 samples, e.g., the shapes of serrations are sharp and blunt for the Z and C6 samples, respectively. These differences in the serration shape may be resourced by the intrinsic brittleness or plasticity of materials. The serrated flow part in the stress−strain curve consists of two parts, that is, the stress drop part, resulting from the shear band sliding and the elastic loading part, resulting from the elastic recovering by the surrounding material and the arresting of the shear-band propagation. It is noteworthy that the elastic recovering for the brittle materials is more difficult, as compared to that for the ductile materials, thereby contributing to the sharp serrations [26,27]. However, the multiple shear bands in the ductile material prohibit the shear band propagation and slow down the shear band propagation velocity, thereby contributing to the blunt serrations. The enhanced plasticity for the C6 sample is related to this fact, which will be discussed in the next sections.

4.2 Fracture surface morphology

Figure 7 shows SEM images of the fracture surface and lateral surface of the Z and C6 fractured samples. As can be seen from Figs. 7(a) and (b), vein-like pattern extending towards the maximum shear stress direction which is typically characteristic of the fracture surface of glassy alloys exists in both fractured samples [28,29].

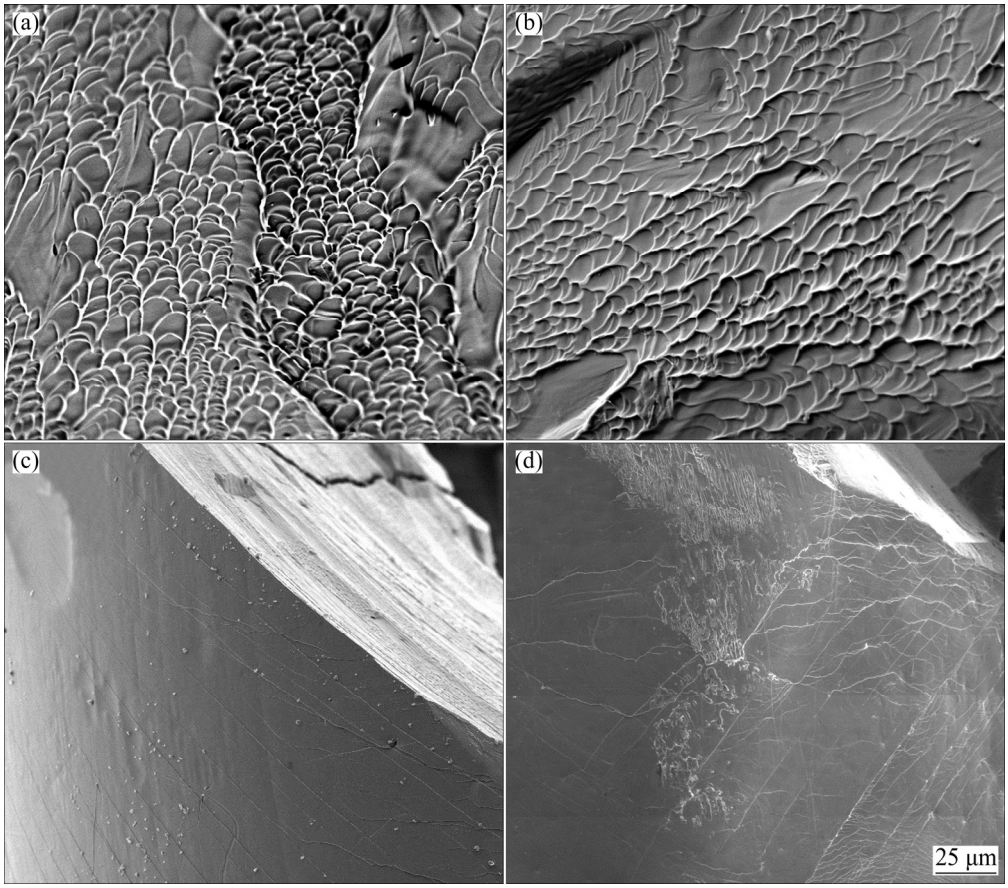

Fig. 7 SEM micrographs of fracture surface (a, b) and lateral surface (c, d) of Z (a, c) and C6 (b, d) samples

The liquid droplets and liquid region have also been observed on the fracture surface of the samples. The locally melted regions observed on the fracture surface suggest a large strain along the shear band [30,31].

The uniform straight primary shear bands for the lateral surface of Z fractured sample could be observed both parallel to each other and also parallel to the fracture direction, as shown in Fig. 7(c). In addition, a number of secondary shear bands with a deviation from the primary shear bands have also been observed. In fact, there exist interactions between the secondary shear bands and primary shear bands.

The illustrations show that the multiple shear bands exist in both samples, but the density of shear bands is different. As can be clearly seen from Fig. 7(d), the density of shear bands for the C6 sample is higher than that for the Z sample, especially the secondary and tertiary shear bands. In some cases, the interactions between the shear bands are responsible for the branching and nucleating of the third new shear bands. Alternatively, the interactions between the shear bands are considerable for this sample. The deformation of BMGs under mechanical loading is highly localized in the shallow shear band region as a result of shear softening. The shear softening in the shear bands results from increasing the free-volume amount and also increasing the heat output due to the elastic energy release. The deformation and shear softening on one main shear band lead to the catastrophic failure without much macroscopic ductility. The multiple shear bands result in the plasticity enhancement by dissipating the shear softening and prohibiting the shear band movement [32]. The plasticity enhancement for the C6 samples is attributed to the shear band pattern characteristic of the multiple shear bands interacting with each other, that is, the branched and proliferated ones.

4.3 Plasticity

It is well-known that the excessive free-volume with heterogeneous distribution in the structure, low-population polyhedral clusters and lower packing regions around the packed polyhedral clusters could act as a fertile site for the shear transformation zones (STZs) [33]. The shear band formation involves cooperative actions of numerous STZs [34]. Thus, more shear bands nucleate by increasing the fertile sites for STZ. The plasticity enhancement through introducing the free-volume in the structure has been studied on different glassy alloys via designing the processing thermal history or alloy composition in previous studies [35,36].

The presence of the free-volume affects the critical shear stress for the shear flow according to the Speapen theory as follows [37]:

$$\sinh \tau_{\max} - \tau_{\max} = G^2 \beta \alpha \gamma v_i^3 \exp(1/v_i) \quad (2)$$

where $\tau_{\max}$ is the critical shear stress, G is the shear modulus, α, β and γ are constants and v_i is the free-volume content. It could be numerically concluded that the critical shear stress decreases dramatically when the free-volume content increases slightly, resulting in the convenient shear flow and numerous shear bands formation.

Based on the structural analysis results and Speapen theory, the excessive free-volume in the structure of the C6 sample, as compared to that of the Z sample could be the main reason for Cu-containing plasticity enhancement.

Another possible reason for increasing the plasticity of the C6 sample may be related to the T_g decrease upon Cu addition. Based on the cooperatives shear model, the activation energy $W(T_g)$ for STZ depends on T_g as follows [38]:

$$W(T_g) = (8/\pi^2)\gamma_c^2 G(T_g) V_m(T_g) \quad (3)$$

where V_m is the molar volume of the alloy and γ_c is constant. It was concluded that the GV_m could be well scaled with the RT_g (R is the mole gas constant), validating the equivalence between $W \propto RT_g$ and $W \propto GV_m$ [39]. Therefore, the T_g decrease causes the activation energy decrease for STZ. Thus, more shear bands nucleate and are distributed in the whole sample by increasing the fertile sites for the STZ, thereby improving the plasticity. In addition, the intrinsic plasticity can be explained by elastic constants. The correlation between the elastic constants and intrinsic plasticity has been widely studied as an interesting subject to succeed in the synthesizing monolithic BMGs with the intrinsic plasticity recently [40,41]. Larger Poisson ratio has been found to have good correlation with the intrinsic plasticity [42,43]. The correlation between elastic constants, including the shear modulus G, bulk modulus B and Poisson ratio υ can be expressed as follows:

$$\upsilon=(3-2G/B)/(6+2G/B) \quad (4)$$

According to Eq. (4), the lower the G/B ratio is, the higher Poisson ratio will be. The lower G/B ratio and higher Poisson ratio were employed for the fracture process of a head of the crack tip. It is well-known that the fracture processes ahead of a crack tip are controlled by the shear flow and dilatation of the material, while the shear modulus captures the resistance to the material shear flow and the bulk modulus embodies the material dilatation.

The nano-indentation test was utilized to measure the elastic constants and the results have been plotted in Fig. 8. The results obtained from the load−displacement (P−h) curves have been summarized in Table 3. As can be seen, the contact stiffness (S) is lower, but the contact area (A), maximum depth ($h_{\max}$) and contact depth (h_c) of the C6 sample are higher than those of the Z sample.

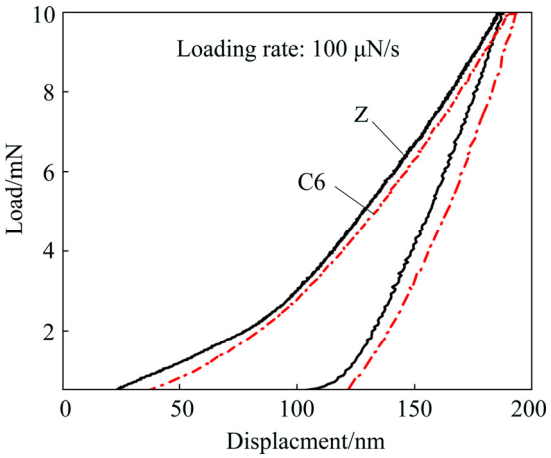

Fig. 8 Load−displacement curve (P−h) obtained from nano indentation test for Z and C6 samples

Table 3 Contact stiffness (S), contact area (A), max depth ($h_{\max}$) and contact depth (h_c) of Z and C6 samples

Sample code	Contact stiffness, S/(μN·nm^{-1})	Contact area, A/nm^2	Max depth, $h_{\max}$/nm	Contact depth, h_c/nm
Z	172.1	743100	187.8	144
C6	166.6	787900	193.7	153.5

The reduced elastic modulus (E_r) can be obtained from the (P−h) curve as follows [44]:

$$S = \frac{dP}{dh} = \frac{2}{\sqrt{\pi}} E_r \sqrt{A} \quad (5)$$

It could be concluded that E_r increases by increasing the contact stiffness and decreasing the contact area. On the other hand, E_r is directly proportional to the elastic modulus (E) as follows [44]:

$$\frac{1}{E_r} = \frac{(1-\upsilon^2)}{E} + \frac{(1-\upsilon_i^2)}{E_i} \quad (6)$$

where E and υ are elastic modulus and Poisson ratio of the material, respectively, and E_i and υ_i are elastic modulus and Poisson ratio of the indenter, respectively. Therefore, it could be concluded that the elastic modulus of C6 sample decreases by increasing the contact area and decreasing the contact stiffness. Thus, according to the direct proportion of elastic modulus and shear modulus, it could be predicted that the G/B ratio decreases and Poisson ratio increases by Cu addition.

In addition, it is noteworthy that Poisson ratio is controlled by two factors, including the average elemental Poisson ratio and the degree of structural ordering [45]. From the average elemental Poisson ratio perspective, it is speculated that the substitution of Co with the Poisson ratio of 0.31 by Cu with a larger Poisson ratio of 0.36 may contribute to an increase in Poisson ratio of the glassy alloy [46]. From the glassy alloy structure perspective, it is expected that the structural evolution effect on the Poisson ratio would be negligible regarding the absence of a remarkable structural change such as short-range ordering. Therefore, it could also be predicted that Poisson ratio increases by Cu addition. In summary, the internal state evolutions such as the excessive free-volume embedded in the structure and the increase of the Poisson ratio may be in good agreement with the intrinsic plasticity of the C6 sample.

5 Conclusions

This work was performed with the aim of fabricating the monolithic BMG with intrinsic plasticity and locating the optimal BMG-forming composition for the quaternary Zr−Co(Cu)−Al glassy alloy. The highest GFA among glassy alloys was found for the $Zr_{56}Co_{22}Cu_6Al_{16}$ alloy, which was similar to that of the base alloy. In addition, the base alloy plasticity increased significantly from ε_p=3.2% to ε_p=6% for the optimized Cu-containing glassy alloy. It was revealed that Cu micro-alloying with the positive mixing enthalpy within Cu and Co elements brings the less dense atomic packing structure with excessive free-volume, thereby contributing to a decrease in liquid viscosity and finally GFA deterioration. However, the reason for the GFA improvement of $Zr_{56}Co_{22}Cu_6Al_{16}$ is the existence of the repulsive interaction between small radium constituents according to Egami model. Furthermore, the convenient activation of more STZ and the convenient nucleation of more shear bands due to the existence of excessive free-volume, the T_g decrease and the Poisson ratio increase are the main reasons for the plasticity enhancement of $Zr_{56}Co_{22}Cu_6Al_{16}$.

Acknowledgements

The authors wish to express their gratitude to Iran University of Science and Technology for the financial support. Also, the authors would like to thank Dr. Reza Gholamipour for his assistance and his laboratory equipment.

References

[1] ZHUANG Y X, WANG S C, WANG C J, WANG N P, HE J C. Effect of Ti on microstructure, mechanical and corrosion properties of $(Zr_{0.55}Al_{0.1}Ni_{0.05}Cu_{0.3})_{100-x}Ti_x$ bulk metallic glasses [J]. Transactions of Nonferrous Metals Society of China, 2016, 26: 138−143.

[2] WU H, BAKER I, LIU Y, WU X L. Dry sliding tribological behavior of Zr-based bulk metallic glass [J]. Transactions of Nonferrous Metals Society of China, 2012, 22: 585−589.

[3] LIN T, HU Y, KONG L T, LI J F. Effect of surface roughness on plasticity of $Zr_{52.5}Cu_{17.9}Ni_{14.6}Al_{10}Ti_5$ bulk metallic glass [J]. Transactions of Nonferrous Metals Society of China, 2012, 22: 1407−1411.

[4] CAI A H, DING D W, AN W K, ZHOU G J, LUO Y, LI J H, PENG Y Y. Transition of plasticity and fracture mode of Zr−Al−Ni−Cu bulk metallic glasses with network structures [J]. Transactions of Nonferrous Metals Society of China, 2015, 25: 2617−2623.

[5] NOLLMAN N, BINKOWSKI I, SCHMIDT V, ROSNER H, WILDE G. Impact of micro-alloying on the plasticity of Pd-based bulk metallic glasses [J]. Scr Mater, 2016, 111: 1−5.

[6] CHEN S, TU J, WU J, HU Q, XIE S, ZOU J. Phase separation and significant plastic strain in a Zr−Cu−Ni−Al−Fe bulk metallic glass [J]. Mater Sci Eng A, 2016, 656: 84−89.

[7] LI J B, JANG J S C, LI C, JIAN S R, TSAI P H, HWANG J D, HUANG J C, NIEH T G. Significant plasticity enhancement of ZrCu-based bulk metallic glass composite dispersed by in-situ and ex-situ Ta particles [J]. Mater Sci Eng A, 2012, 551: 249−254.

[8] CHEN L Y, SETAYAWAN A D, KATO H, INOUE A, ZHANG G Q, SAIDA J, WANG X D, CAO Q P, JIANG J Z. Free-volume-induced enhancement of plasticity in a monolithic bulk metallic glass at room temperature [J]. Scr Mater, 2008, 59: 75−78.

[9] ABBASI M, GHOLAMIPOUR R, SHAHRI F. Glass forming ability and mechanical properties of Nb-containing Cu−Zr−Al based bulk metallic glasses [J]. Transactions of Nonferrous Metals Society of China, 2013, 23: 2037−2041.

[10] LIU G Q, KOU S Z, LI C Y, ZHAO Y C, SUO H L. Effect of minor Fe addition on glass forming ability and mechanical properties of $Zr_{55}Al_{10}Ni_5Cu_{30}$ bulk metallic glass [J]. Transactions of Nonferrous Metals Society of China, 2012, 22: 590−595.

[11] HUA N, HUANG L, WANG J, CAO Y, HE W, PANG S, ZHANG T. Corrosion behavior and in vitro biocompatibility of Zr−Al−Co−Ag bulk metallic glasses: An experimental case study [J]. J Non Cryst Solids, 2012, 358: 1599−1604.

[12] WANG R, WANG Y, YANG J, SUN J, XIONG L. Influence of heat treatment on the mechanical properties, corrosion behavior, and biocompatibility of $Zr_{56}Al_{16}Co_{28}$ bulk metallic glass [J]. J Non Cryst Solids, 2015, 411: 45−52.

[13] WADA T, QIN F, WANG X, YOSHIMURA M, INOUE A, SUGIYAMA N, ITO R, MATUSHITA N. Formation and bioactivation of Zr−Al−Co bulk metallic glasses [J]. J Mater Res, 2009, 24: 2941−2948.

[14] ZHANG T, INOUE A. Formation, thermal and mechanical properties of bulk glassy alloys in Zr−Al−Co and Zr−Al−Co−Cu systems [J]. Mater Sci Eng A, 2004, 375: 432−435.

[15] INOUE A. Stabilization of metallic supercooled liquid and bulk amorphous alloys [J]. Acta Mater, 2009, 48: 279−306.

[16] INOUE A. Mechanical properties of Zr-based bulk glassy alloys containing nanoscale compound particles [J]. Intermetallics, 2000, 8: 455−468.

[17] CUI X, ZU F Q, JIANG W X, WANG L F, WANG Z Z. Achieving superior glass forming ability of Zr−Cu−Al−Ni−Ti/Ag bulk metallic glasses by element substitution [J]. J Non Cryst Solids, 2013, 375: 83−87.

[18] SUO Z Y, QIU K Q, LI Q F, YOU J H, REN Y L, HU Z Q. A new parameter to evaluate the glass-forming ability of bulk metallic glasses [J]. Mater Sci Eng A, 2010, 528: 429−433.

[19] SURYANARAYANA C, INOUE A. Bulk metallic glasses [M]. Abingdon: Taylor and Francis Group, 2009.

[20] BLYSKUN P, MAJ P, KOWALCZYK M, LAUTUCH J, KULIIK T. Relation of various GFA indicators to the critical diameter of Zr-based BMGs [J]. J Alloys Compd, 2015, 625: 13−17.
[21] ZHANG Q, ZHANG W, INOUE A. Unusual glass-forming ability of new Zr−Cu-based bulk glassy alloys containing an immiscible element pair [J]. Mater Trans, 2008, 49: 2743−2746.
[22] EGAMI T. Atomistic mechanism of bulk metallic glass formation [J]. J Non Cryst Solids, 2003, 317: 30−33.
[23] LIU Z, CHAN K C, LIU L. Enhanced glass forming ability and plasticity of a Ni-free Zr-based bulk metallic glass [J]. J Alloys Compd, 2009, 487: 152−156.
[24] ZHANG C, LI N, PAN J, GUO S F, ZHANG M, LIU L. Enhancement of glass-forming ability and bio-corrosion resistance of Zr−Co−Al bulk metallic glasses by the addition of Ag [J]. J Alloys Compd, 2010, 504: 163−167.
[25] GREER A L. Confusion by design [J]. Nature, 1993, 366: 303−304.
[26] MA G Z, SUN B A, PAULY S, SONG K K, KUHN U, CHEN D, ECKERT J. Effect of Ti substitution on glass-forming ability and mechanical properties of a brittle Cu−Zr−Al bulk metallic glass [J]. Mater Sci Eng A, 2013, 563: 112−116.
[27] HU J, SUN B A, YANG Y, LIU C T, PAULY S, WENG Y X, ECKERT J. Intermetallics Intrinsic versus extrinsic effects on serrated flow of bulk metallic glasses [J]. Intermetallics, 2015, 66: 31−39.
[28] GREER A L, CHENG Y Q, MA E. Shear bands in metallic glasses [J]. Mater Sci Eng R, 2013, 74: 71−132.
[29] TREXLER M M, THADHANI N N. Mechanical properties of bulk metallic glasses [J]. Prog Mater Sci, 2010, 55: 759−839.
[30] LI J B, JANG J S C, JIAN S R, CHEN K W, LIN J F, HUANG J C. Plasticity improvement of ZrCu-based bulk metallic glass by ex situ dispersed Ta particles [J]. Mater Sci Eng A, 2011, 528: 8244−8248.
[31] KHADEMIAN N, GHOLAMIPOUR R, SHAHRI F, TAMIZIFAR M. Effect of vanadium substitution for zirconium on the glass forming ability and mechanical properties of a $Zr_{65}Cu_{17.5}Ni_{10}Al_{7.5}$ bulk metallic glass [J]. J Alloys Compd, 2013, 546: 41−47.
[32] LOUZGUINE LUZGINA D, LOUZGUINE LUZGINA L, CHURYMOV A. Mechanical properties and deformation behavior of bulk metallic glasses [J]. Metals, 2012, 3: 1−22.
[33] ZHU Z W, GU L, XIE G Q, ZHANG W, INOUE A, ZHANG H F, HU Z Q. Relation between icosahedral short-range ordering and plastic deformation in Zr−Nb−Cu−Ni−Al bulk metallic glasses [J]. Acta Mater, 2011, 59: 2814−2822.
[34] HU Y, YAN H H, LIN T, LI J F, ZHOU Y H. Effect of cooling rate on the bending plasticity of $Zr_{55}Al_{10}Ni_5Cu_{30}$ bulk metallic glass [J]. J Alloys Compd, 2012, 527: 36−39.
[35] WU H, LIU Y, LI K Y, ZHAO Z W. Casting effect on compressive brittleness of bulk metallic glass [J]. Transactions of Nonferrous Metals Society of China, 2014, 24: 385−392.
[36] ZHU S, XIE G, WANG H, YANG X, CUI Z, INOUE A. Zr-based bulk metallic glass composite with in situ precipitated nanocrystals [J]. J Alloys Compd, 2014, 586: 155−158.
[37] HUTCHINSON J W, SPEAPEN F. Strain localization in amorphous metals [J]. Acta Met, 1982, 30: 447−455.
[38] JOHNSON W L, SAMWER K. A universal criterion for plastic yielding of metallic glasses with a $(T/T_g)_{2/3}$ temperature dependence [J]. Phys Rev Lett, 2005, 95: 2−5.
[39] HE Q, XU J. Locating malleable bulk metallic glasses in Zr−Ti−Cu−Al alloys with calorimetric glass transition temperature as an indicator [J]. J Mater Sci Technol, 2012, 28: 1109−1122.
[40] CHENG Y Q, CAO A J, MA E. Correlation between the elastic modulus and the intrinsic plastic behavior of metallic glasses: The roles of atomic configuration and alloy composition [J]. Acta Mater, 2009, 57: 3253−3267.
[41] LEWANDOWSKI J J, SHAZLY M, NOURI A S. Intrinsic and extrinsic toughening of metallic glasses [J]. Scr Mater, 2006, 54: 337−344.
[42] HUA N, LI G, LIN C, YE X, WANG W, CHEN W. Chemistry effects on the compressive property and Weibull modulus of Zr-based bulk metallic glasses [J]. J Non-Cryst Solids, 2015, 15: 342−347.
[43] HE Q, CHENG Y Q, MA E, XU J. Locating bulk metallic glasses with high fracture toughness: Chemical effects and composition optimization [J]. Acta Mater, 2011, 59: 202−215.
[44] OLIVER W, PHARR G. An improved technique for determining hardness and elastic modulus using load and displacement sensing indentation experiments [J]. J Mater Res, 1992, 7: 1564−1583.
[45] CHENG Y Q, MA E. Atomic-level structure and structure-property relationship in metallic glasses [J]. Prog Mater Sci, 2011, 56: 379−473.
[46] ZHANG Y, GREER A L. Correlations for predicting plasticity or brittleness of metallic glasses [J]. J Alloys Compd, 2007, 434: 2−5.

具有最优玻璃形成能力的 Zr−Co(Cu)−Al 大块金属玻璃及其压缩性能

Masoud MOHAMMADI RAHVARD, Morteza TAMIZIFAR, Seyed Mohammad Ali BOUTORABI

School of Materials Science and Engineering, Center of Excellence for High Strength Alloys Technology, Iran University of Science and Technology, Tehran 1684613114, Iran

摘　要：采用铜模吸铸法在三元 $Zr_{56}Co_{28}Al_{16}$ 和四元 $Zr_{56}Co_{28-x}Cu_xAl_{16}$ (x=2，4，5，6，7，摩尔分数，%)非晶合金中形成大块金属玻璃(BMGs)。本研究主要目的是找到四元 ZrCo(Cu)Al 合金中形成大块金属玻璃的最优成分，并提高母合金的塑性。采用 X 射线衍射(XRD)技术、透射电镜(TEM)和差示扫描量热法(DSC)研究非晶合金的结构及其玻璃形成能力(GFA)。此外，利用压缩试验、显微硬度、纳米压痕和扫描电镜(SEM)讨论塑性提高的可能机制。含铜合金中玻璃形成能力最强的是 $Zr_{56}Co_{22}Cu_6Al_{16}$ 合金，与基体合金相似。此外，$Zr_{56}Co_{22}Cu_6Al_{16}$ 大块金属玻璃的塑性从基体合金的 3.3%显著增加到 6%。最后，结合铜和钴的正混合热，讨论合金塑性和 GFA 的变化。

关键词：大块金属玻璃；锆基合金；玻璃形成能力；塑性

(Edited by Wei-ping CHEN)